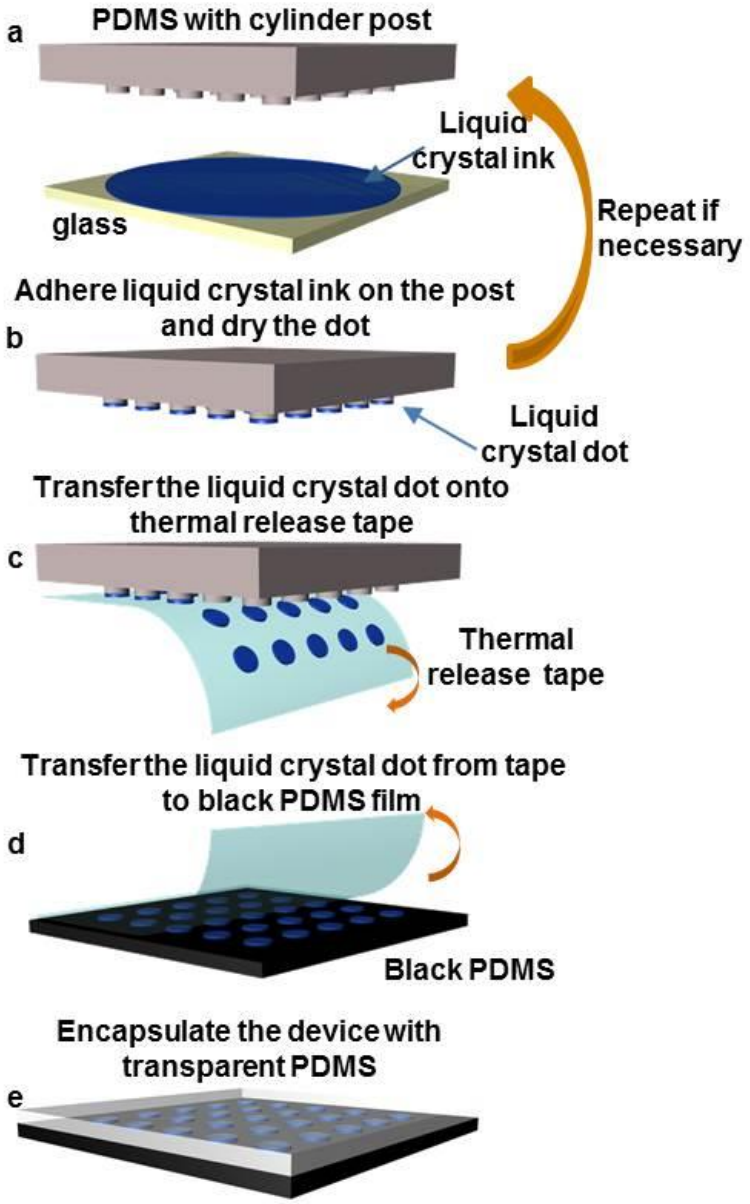

Supplementary Figure 1: Process for fabricating e-TLC devices. (**a**) A PDMS stamp with an array of posts embossed on its surface is 'inked' by bringing it into contact with a uniform layer of TLC aqueous slurry spin cast on a glass slide while still in wet state. The thickness of the ink was ~100 μm to ensure that the ink contacts on the top surfaces of the posts. (**b**) The inked TLC material on the PDMS stamp was allowed to dry in air for 15 minutes. The thickness of the dried film is ~15 μm. Additional 'inking' processes are repeated to achieve a final thickness of 25-30μm. A typical TLC pixel is thickest in the center due to the hydrophobic nature of the PDMS surface and the large contact angle formed during the inking process. (**c**) Transfer printing allows delivery of the TLC to a piece of thermal release tape. (**d**) Transfer to the black PDMS substrate is enabled by heat activated release from the tape. (**e**) The device is encapsulated with a transparent layer of PDMS by spin casting.

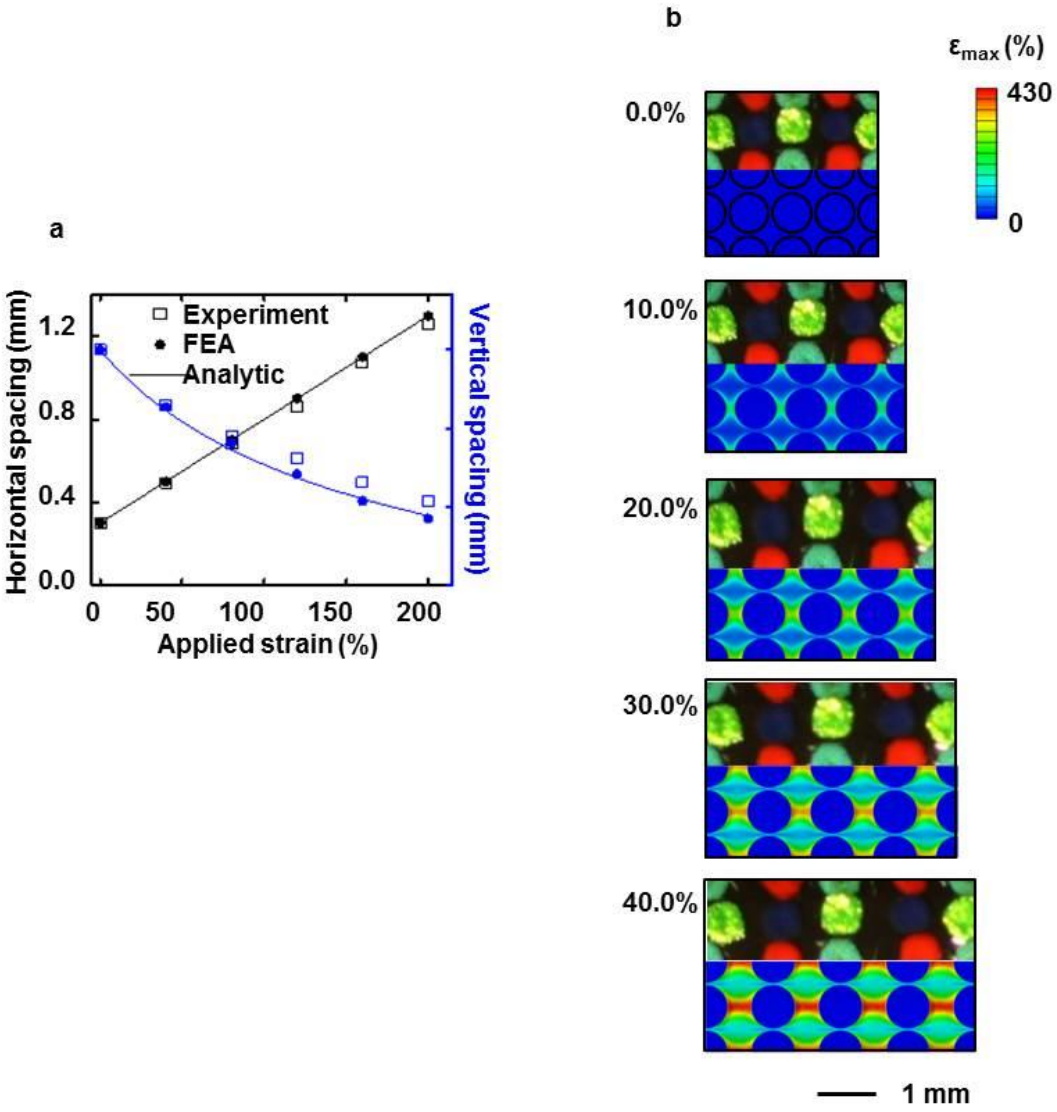

Supplementary Figure 2: Mechanical response of an e-TLC device to uniaxial strain. (**a**) Experimental, analytical and finite element modeling results for the change in horizontal and vertical spacings between adjacent pixels under different levels of tensile strain. (**b**) Comparison between images and three dimensional finite element modeling of a representative region of an e-TLC device that incorporates color calibration pixels under different levels of tensile strain.

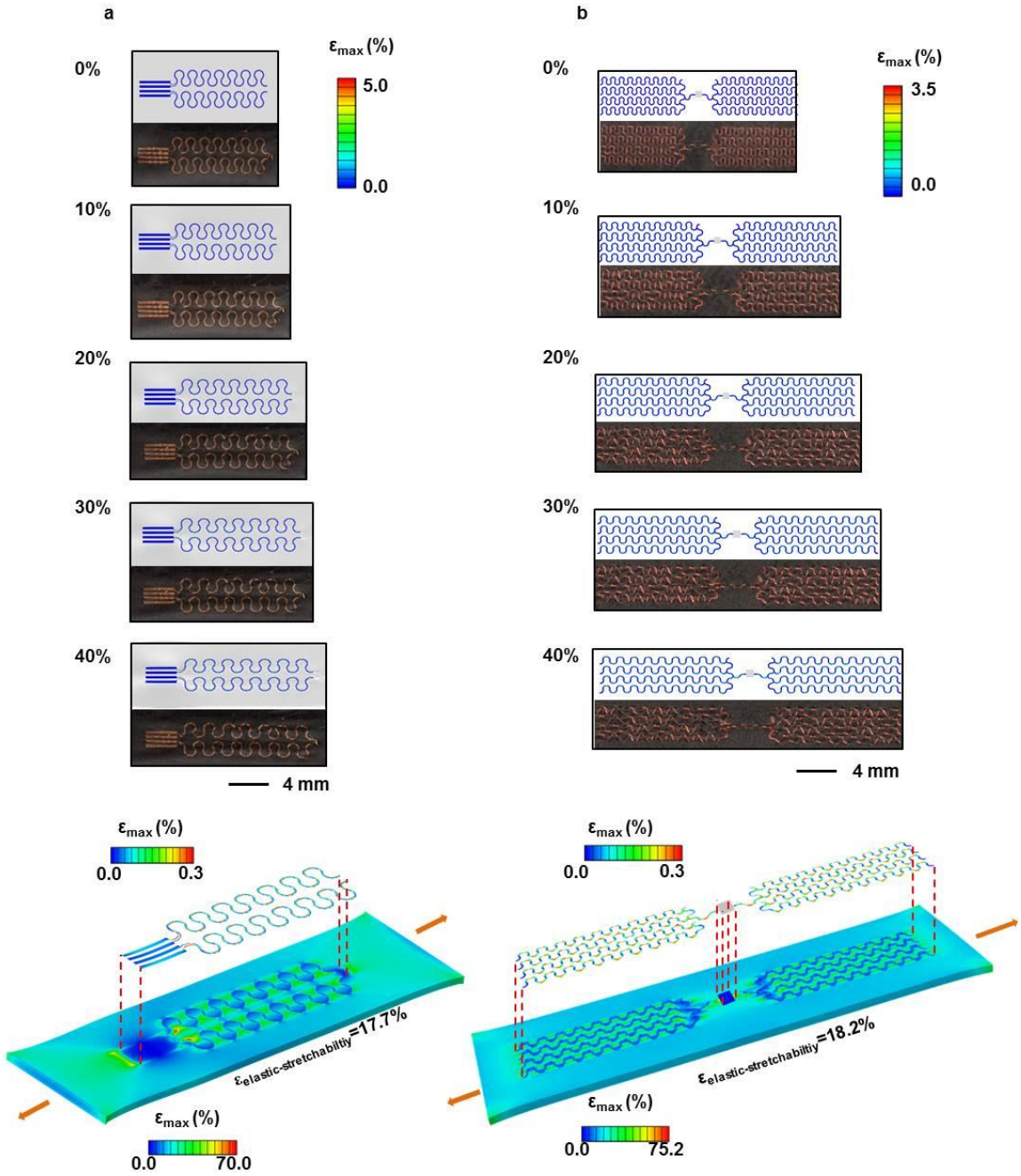

Supplementary Figure 3: Experimental and computational studies of the mechanical properties of Joule heater element. (**a**) Comparison between experimental images and three dimensional finite element modeling of a wired Joule heating element under different levels of tensile strain, and strain distribution computed for the case of stretching to 50%. (**b**) Comparison between experimental images and three dimensional finite element modeling of a wireless Joule heater under different levels of tensile strain, and strain distribution computed for the case of stretching to 50%.

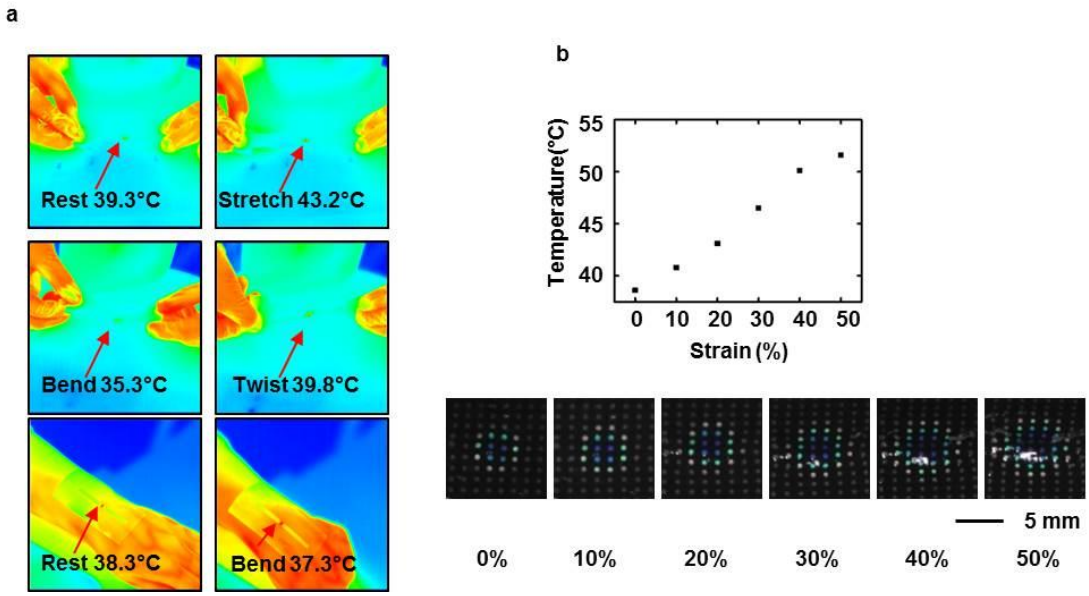

Supplementary Figure 4: Experimental studies of the effect of strain on the efficiency of wireless Joule heating. (**a**) Infrared temperature measurements for a wireless Joule heater under exposure to RF energy while mechanically deformed in different ways, both in air and on skin. (**b**) Measurements at different levels of tensile strain with corresponding images.

a

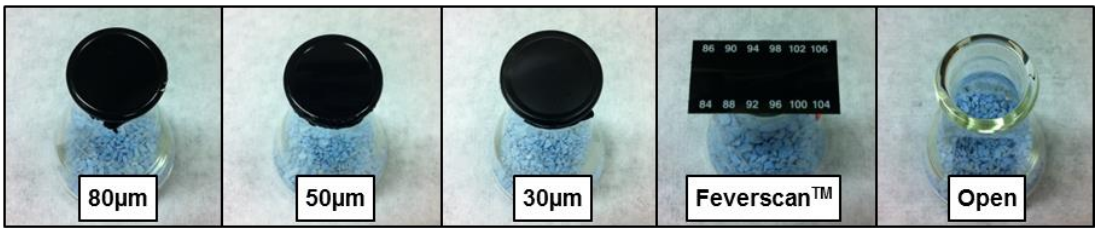

b

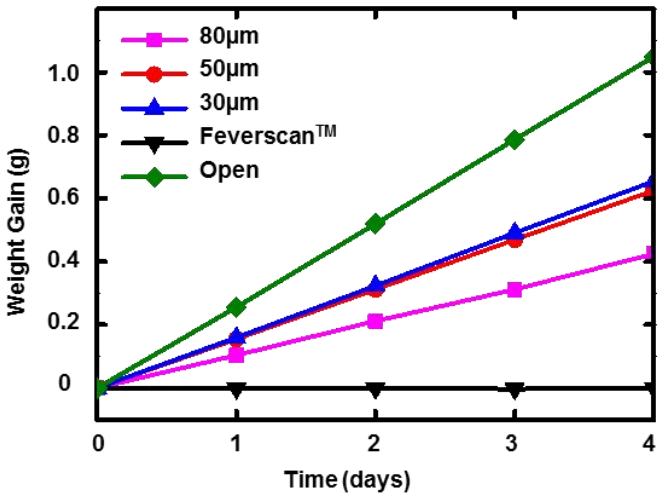

Supplementary Figure 5: Water permeability test. (**a**) Images of the experimental set-ups for measurement of water permeation according to ASTM E96-95 guidelines, and (**b**) Results of the change in weight as a function of time associated with water uptake by the dessicant, for e-TLC devices with different thicknesses and for a commercial TLC strip.

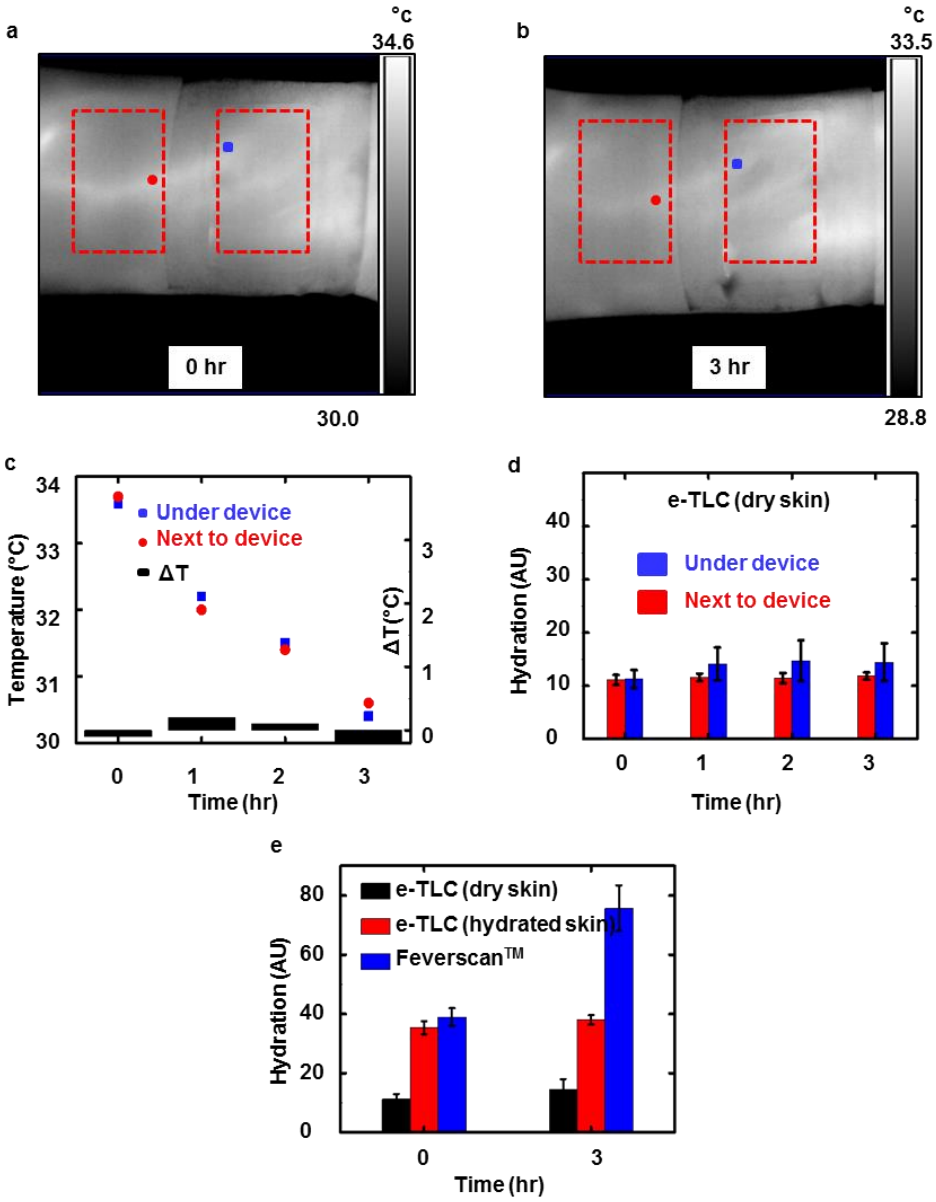

Supplementary Figure 6: Effect of e-TLC operation on temperature and hydration of the skin. (**a**) Infrared image captured immediately after mounting an e-TLC device on the wrist. (**b**) Infrared image captured 3 hours after mounting. For both (a) and (b), the data indicate that the average temperatures at the regions of the device are the same as those adjacent to the device. (**c**) Temperature difference between a point near the device and a point underneath the device shows no obvious increase during the three hour operation. (**d**) Measurement of hydration using a Delfin meter in a region of dry skin (baseline reading ~10) after 3 hours of contact with an 80 μm thick e-TLC indicates an increase of ~25%. (**e**) The same device, under identical conditions, on well hydrated skin (baseline reading ~35) leads to much smaller percentage increases (7.5%). For an otherwise identical set of testing conditions, the Feverscan™ strip led to a ~100% increase in the hydration.

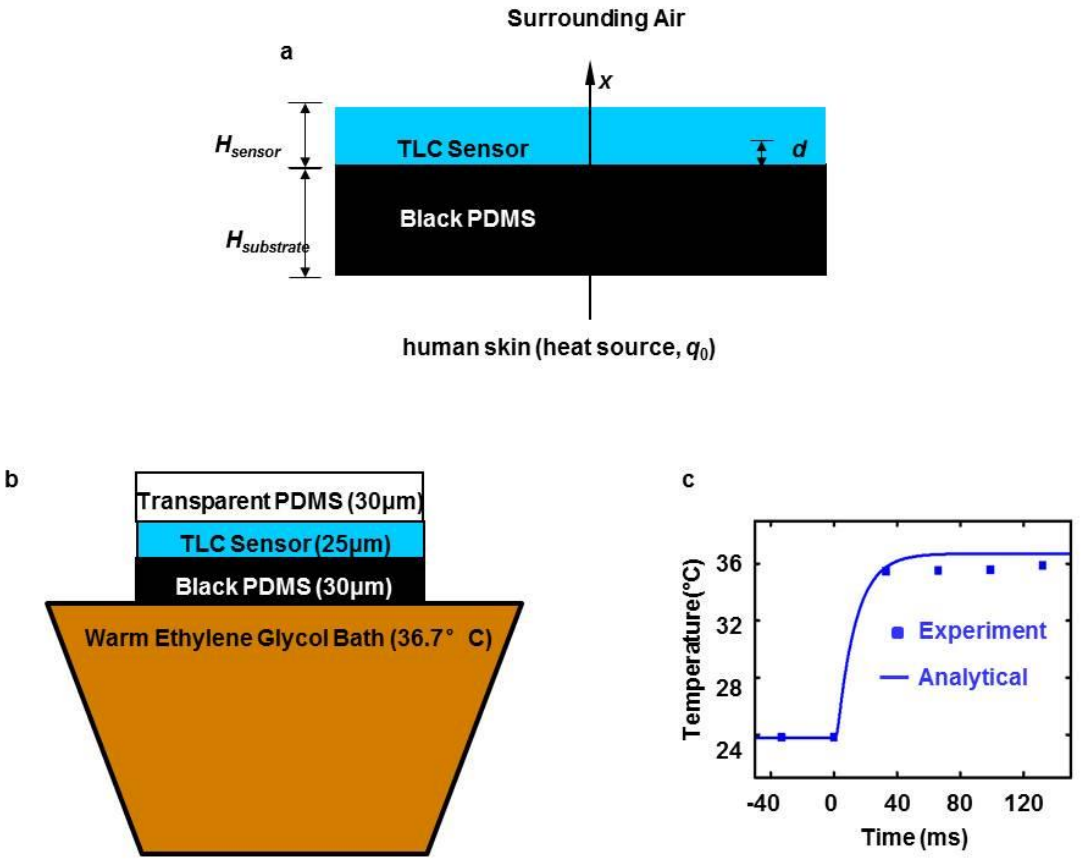

Supplementary Figure 7: Sensor response time. (**a**) Layers used in analytical modeling to determine sensor response time on skin. (**b**) Experimental setup for measuring sensor response time. A warm ethylene glycol bath, which has similar thermal properties to skin, is in contact with the e-TLC device from the back surface. (**c**) Experimental sensor response time captured by high speed camera, and corresponding analytic predictions based on a one-dimensional heat conduction model. In experiment, the time required for the sensor to reach 90% of the total temperature change is achieved in one frame which is approximate 33 ms for the case of 30μm black PDMS and 25μm liquid crystal.

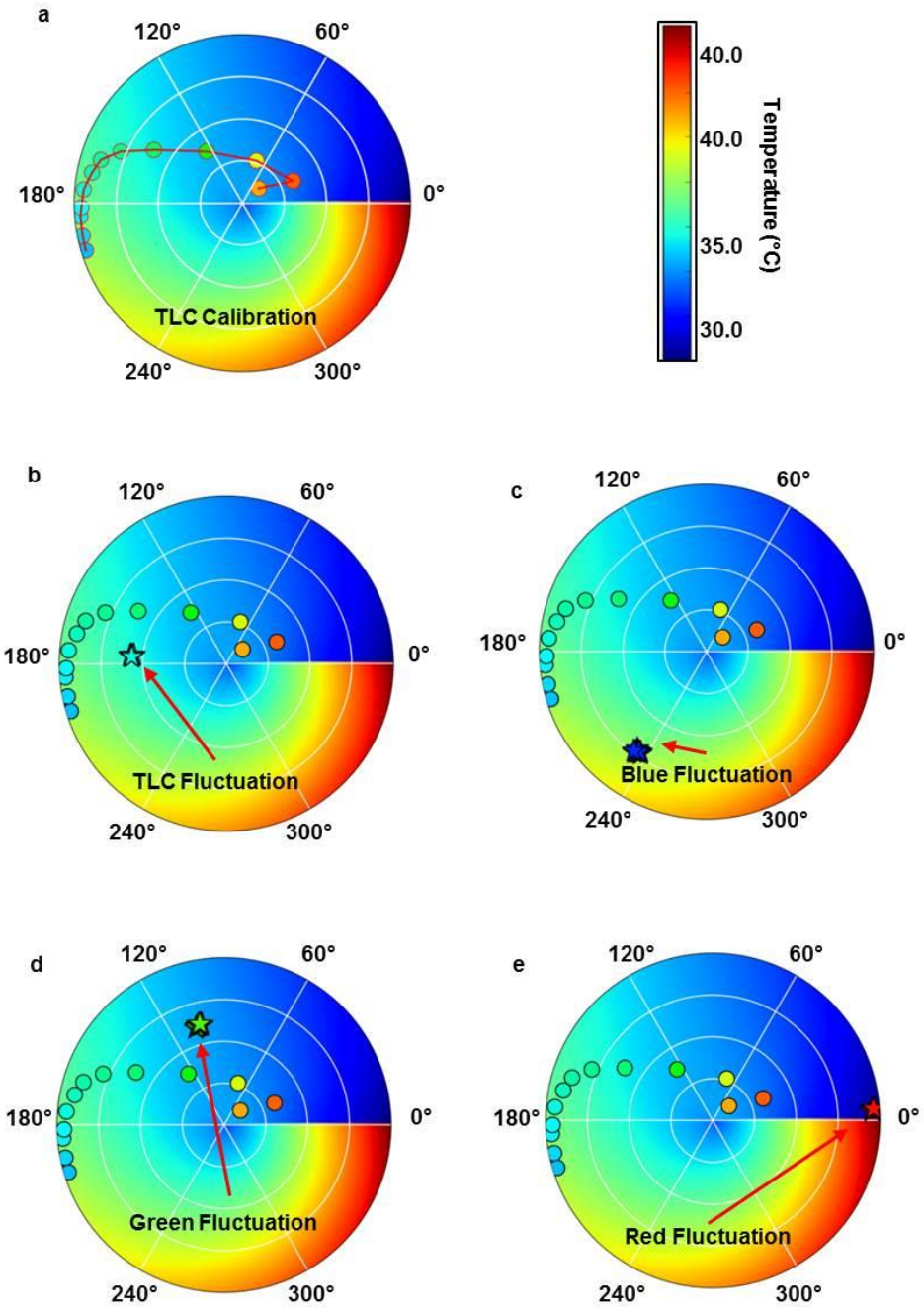

Supplementary Figure 8: Noise and uncertainty examined using temperature insensitive acrylic colors. (**a**) TLC color-temperature calibration plotted in the hue/saturation space. Symbols are located at positions corresponding to the hue/saturation values of the TLC during calibration runs, as indicated with their hue values. Temperatures are calculated with a two dimensional linear fit and are represented by a color gradient. (**b**) Temporal fluctuation in the color of the TLC, when held at a nominally fixed temperature. (**c**) Temporal fluctuation of the blue calibration color at fixed temperature. (**d**) Temporal fluctuation of the green calibration color at fixed temperature. (**e**) Temporal fluctuation of the red calibration color at fixed temperature.

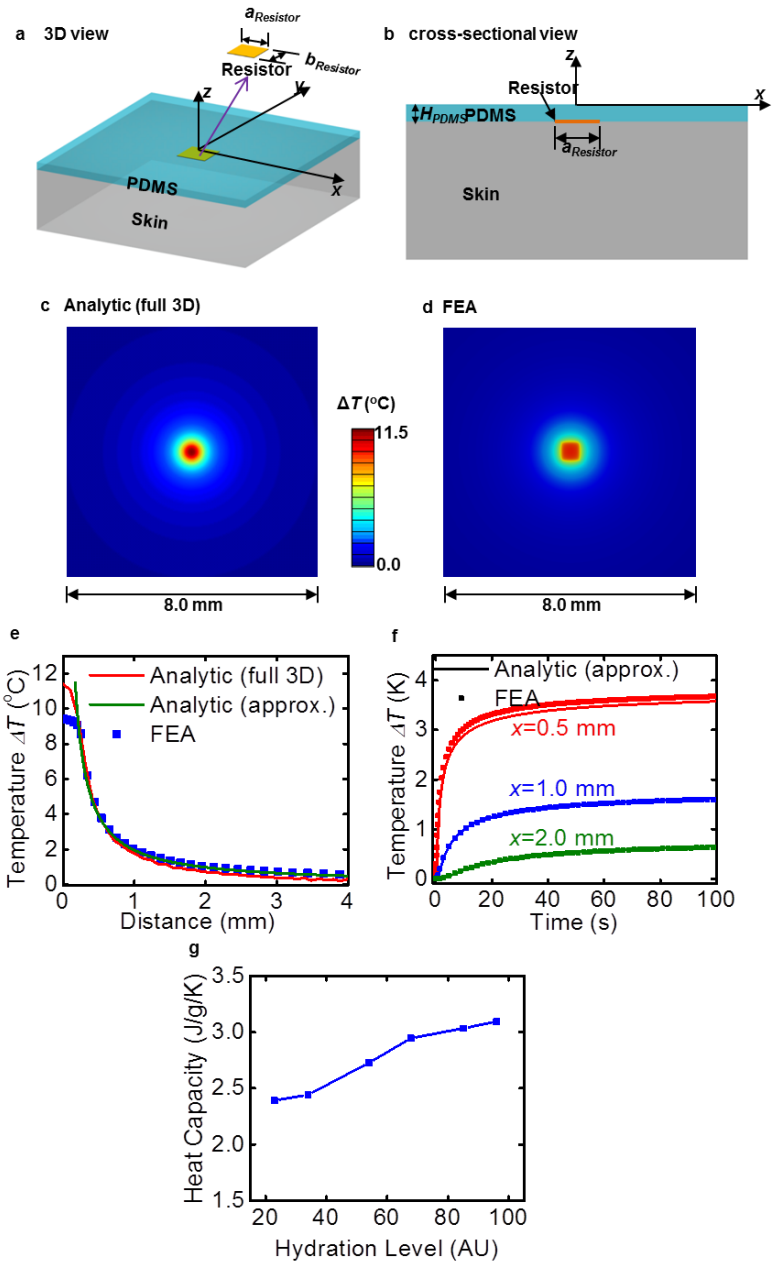

Supplementary Figure 9: Finite element models that allow determination thermal conductivity and diffusivity from data collected using active e-TLC devices. (**a**) A 3D view of a model with a Joule heater embedded between an e-TLC device and the skin. (**b**) A cross-sectional view of a model with a Joule heater embedded between an e-TLC device and the skin. (**c**) Analytical model of the spatial decay in temperature at steady state during operation of the Joule heater. (**d**) Corresponding finite element modeling results. (**e**) Analytical and finite element model of the spatial temperature decay with a wired Joule heater operation along one dimension. (**f**) Analytical and finite element model of the temporal temperature rise with a wireless Joule heater operation for locations away from the heater. (**g**) Skin heat capacity inferred from the skin thermal conductivity and diffusivity values in Figure 5.

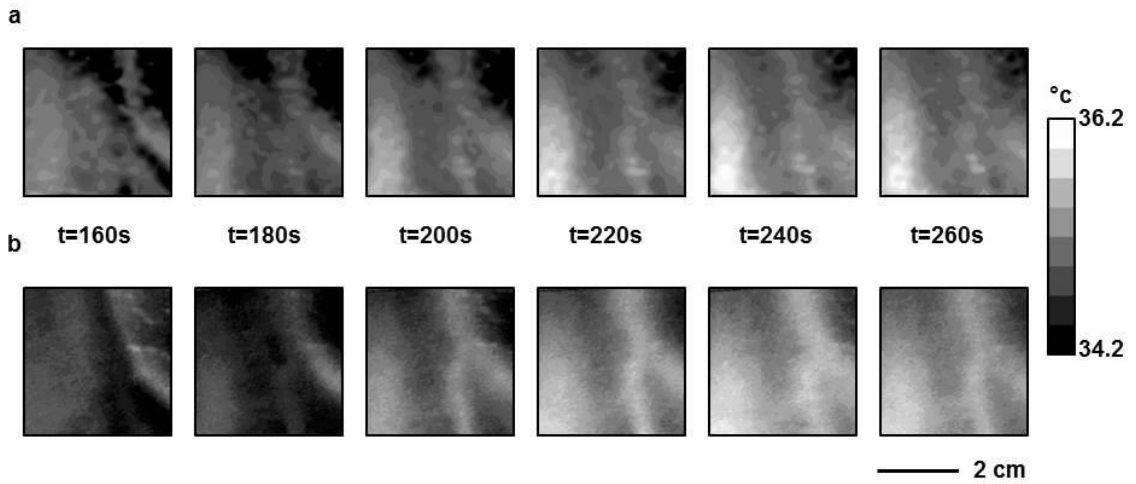

Supplementary Figure 10: Comparison of an e-TLC thermal imaging device and infrared camera measurement in a reactive hyperaemia test. (**a**) Spatial distributions of temperature determined with the e-TLC device at representative times from t=160s to t=260s at an interval of 20s. (**b**) Spatial distributions of temperature determined with the infrared camera at representative times from t=160s to t=260s at an interval of 20s.

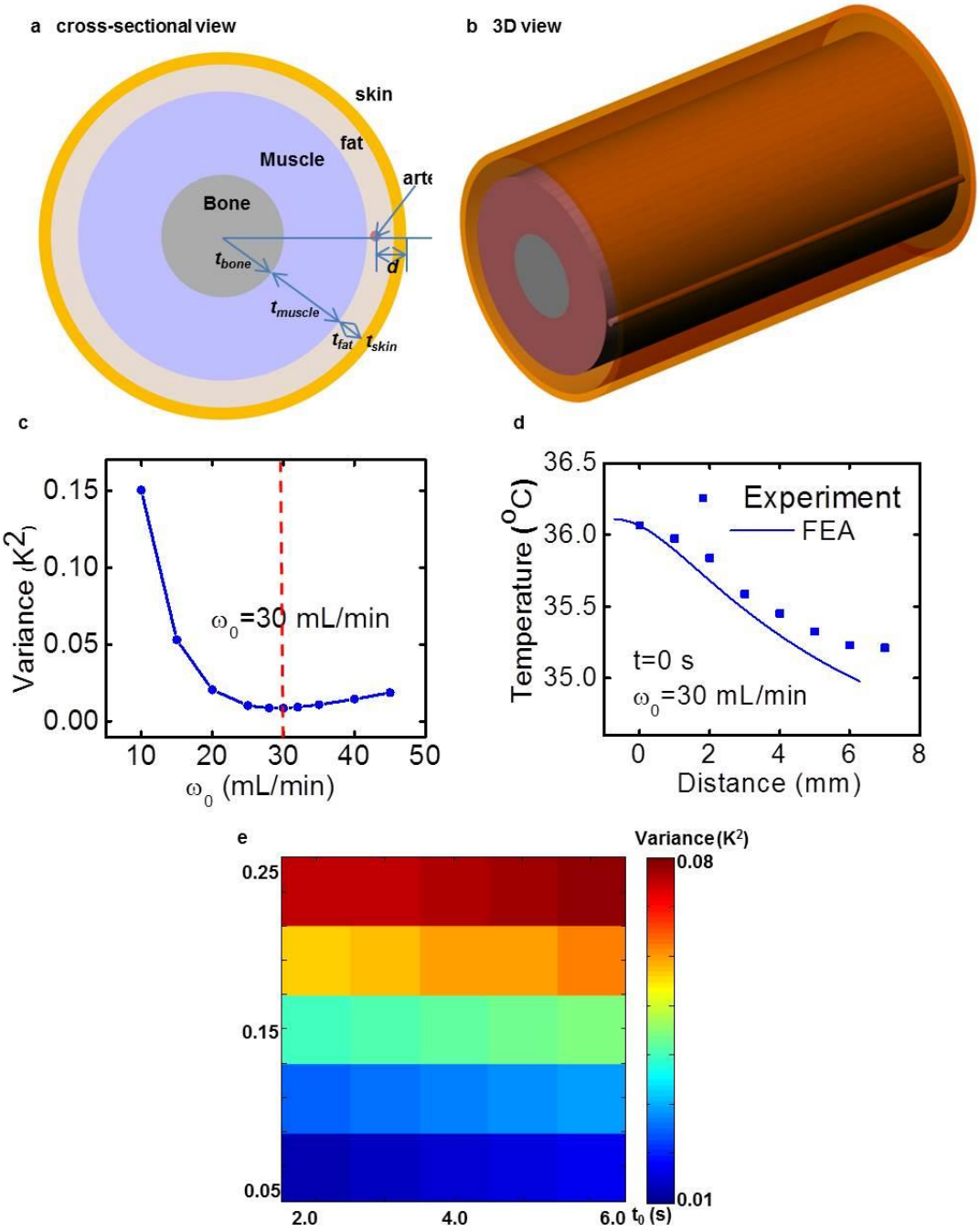

Supplementary Figure 11: Schematic illustration of the thermal conduction model that determines the blood flow rate during occlusion. (**a**) Cross-sectional view and (**b**) three-dimensional view of the wrist model; (**c**) Temperature variance of FEA and experiment versus the baseline flow rate; (**d**) Experimental results of the steady-state temperature as a function of the distance from the artery, as compared to the FEA calculations using the baseline flow rate of 30 mL/min; (**e**) Distribution of temperature variance in the space of parameters, α and τ_0, during stage II of occlusion.

Supplementary Table 1. The parameter range in the model of reactive hyperemia for simulations.

	ω_0 (mL/min)	$\alpha=\omega_s/\omega_0$	$\beta=\omega_{max}/\omega_0$	τ_0(s)	t_{dw} (s)	τ_h(s)
Range	[10, 45]	[0.05, 0.25]	[3, 10]	[2, 6]	[15, 45]	[35, 75]

Supplementary Table 2. The geometric and thermal-physical properties of various tissues for the wrist, where *t* denotes the thickness, *D* is the diameter of the artery, and *d* is the depth of the artery.

Parameter	Skin	Fat	Muscle	Bone	Blood
ρ (kg/m^3)[2,4]	1085	850	1085	1357	1069
c_p (J/kg/K) [2,4]	3680	2300	3768	1700	3659
k (W/m/K) [5,7]	0.47	0.16	0.42	0.75	/
t (mm) [5-7]	1.0	4.4	13.6	10.0	/
D (mm) [8]	/	/	/	/	1.8
d (mm) [9,10]	/	/	/	/	2.2

Supplementary Note 1:

Fabrication procedure for PDMS post stamp used for inking liquid crystal

1. Clean a 3” Si wafer (Acetone, IPA -> Dry 5 min at 110 °C).

2. Spin coat SU8 50 (microchem, 1000rpm for 30s, anneal 65°C 10min 95°C 30min)

3. Pattern SU8 with 365nm optical lithography through iron oxide mask (Karl Suss MJB3) develop in SU8 developer

4 post exposure bake at 65°C 1min 95°C 10min

5. STS ICP RIE silicon etch SF6 20s at 20w CF4 10s at 0w for 250cycles to achieve a hole depth of around 400um

6. Mold the silicon template with PDMS

Fabrication procedure for a single heater with wired and wireless design

Prepare polymer base layers

1. Clean a 3” Si wafer (Acetone, IPA -> Dry 5 min at 110 °C).

2. Spin coat with PMMA (poly(methyl methacrylate), spun at 3,000 rpm for 30 s).

3. Anneal at 180 °C for 10 min.

4. Spin coat with polyimide (PI, poly(pyromellitic dianhydride-co-4,4′ -oxydianiline), amic acid solution, Sigma-Aldrich, spun at 4,000 rpm for 30 s for wired design and 1,000 rpm for 30s for wireless design).

5. Anneal at 110 °C for 30 s.

6. Anneal at 150 °C for 5 min.

7. Anneal at 250 °C under vacuum for 1 hr.

Deposit first metallization

8. E-beam 5/50 nm Cr/Au.

9. Pattern photoresist (PR; Clariant AZ5214, 3000 rpm, 30s) with 365 nm optical lithography through iron oxide mask (Karl Suss MJB3).

Develop in aqueous base developer (MIF 327).

10. Etch Au with TFA Au etchant (Transene).

11. Etch Cr with CR-7 Cr Mask Etchant (Cyantek).

12. Remove PR w/ Acetone, IPA rinse.

13. Dry 5 min at 150 °C.

Isolate first metallization and pattern via holes

14. Spin coat with PI.

15. Anneal at 110 °C for 30 s.

16. Anneal at 150 °C for 5 min.

17. Anneal at 250 °C under vacuum for 1 hr.

18. Pattern photoresist (PR; Clariant AZ4620, 3000 rpm, 30s;) with 365 nm optical lithography through iron oxide mask (Karl Suss MJB3). Develop in aqueous base developer (AZ 400K, diluted 3:1).

19. Reactive ion etch (RIE; March CS-1701, 50 mTorr, 20 sccm O2, 150 W, 35 min).

Deposit second metallization

20. E-beam 5/500 nm Cr/Au for wired design or 5/1600nm Cr/Cu for wireless design.

21. Pattern PR AZ5214.

22. Etch Au with TFA Au etchant or etch Cu with TFA Cu etchant.cs

23. Etch Cr with Cr Mask Etchant.

24. Remove PR w/ Acetone, IPA rinse.

25. Dry 5 min at 150 °C.

Isolate entire device

26. Spin coat with PI.

27. Anneal at 110 °C for 30 s.

28. Anneal at 150 °C for 5 min.

29. Anneal at 250 °C under vacuum for 1 hr.

30. Pattern PR AZ4620.

31. RIE (50 mTorr, 20 sccm O2, 150 W, 35 min for wired design and 120 min for wireless design).

Release and transfer

32. Release w/ boiling Acetone.

33. Transfer to water soluble tape.

34. E-beam 3/30 nm Ti/SiO2.

35. Transfer to back of e-TLC device.

36. Bond thin, flexible cable (Elform, HST-9805-210) using hot iron with firm pressure for wired heater

Supplementary Note 2: Analytic solution of spacing of e-TLC dots during uniaxial stretching

The deformation of an e-TLC device under uniaxial stretching (along horizontal direction) is analyzed to determine the change of spacing between pixels associated with the applied strain (ε). The e-TLC material (~221 MPa) is much

stiffer than the elastomeric substrate (~131 kPa), and therefore undergoes negligible deformation, as evidenced by the experiment images of FEA results in Fig. 2b. The stretching deformation is, as a result, mainly accommodated by the soft substrate material. For pixels (in diameter of d_{TLC}) with an initial spacing Δ_0, the horizontal spacing ($\Delta_{horizontal}$) after deformation is given by

$$\Delta_{horizontal} = \Delta_0 + \left(\Delta_0 + d_{TLC}\right)\varepsilon . \quad (1)$$

The vertical spacing ($\Delta_{vertical}$) decreases due to the Poisson effect. For sparsely distributed pixels (e.g., $d_{TLC} < \Delta_0$), the mechanical constrains associated with the e-TLC on the transverse compression can be neglected, such that the vertical spacing ($\Delta_{vertical}$) after deformation can be approximated as

$$\Delta_{vertical} = \frac{\Delta_0 + d_{TLC}}{\sqrt{1+\varepsilon}} - d_{TLC} . \quad (2)$$

Note that the transversely compressive strain of the soft substrate, due to stretching (ε), is given by $\varepsilon_{compression} = 1-\left(1+\varepsilon\right)^{-1/2}$, since it is nearly incompressible (i.e., Poisson ratio v=0.5). For $\Delta_0 = 0.3\ \text{mm},\ d_{TLC} = 0.2\ \text{mm}$, as adopted in experiments, the analytic results in Fig. S2a, based on Eqs. (S1) and (S2), agree well with the experiment and FEA results.

Supplementary Note 3: Thermal mass calculation of e-TLC device

The thermal mass of the devices are determined for 20 μm silicone and black iron oxide substrate and 30μm transparent silicone substrate. The devices have an overall aerial coverage of ~15 cm^2. The calculated thermal masses that follow

are given as thermal mass per unit area of skin. The device construction for the TCR device contains approximately 8.7 $ng \cdot cm^{-2}$ of Au, 56 $\mu g \cdot cm^{-2}$ of PI, 55.8 $\mu g \cdot cm^{-2}$ of Cu, 0.64 $mg \cdot cm^{-2}$of black iron oxide powder, 4.18 $mg \cdot cm^{-2}$ of silicone substrate, ~0.61 $mg \cdot cm^{-2}$ of liquid crystal materials (Hallcrest, density 0.97$g \cdot cm^{-3}$). The material contributions to aerial thermal mass are: 21.48 $\mu J \cdot cm^{-2} \cdot K^{-1}$ from Cu, 64.4 $\mu J \cdot cm^{-2} \cdot K^{-1}$ from PI, 0.42 $mJ \cdot cm^{-2} \cdot K^{-1}$ from black iron oxide, ~1.09 $mJ \cdot cm^{-2} \cdot K^{-1}$ from liquid crystal (Hallcrest, specific heat Specific heat 1.8 $J \cdot g^{-1} \cdot K^{-1}$), 6.11 $mJ \cdot cm^{-2} \cdot K^{-1}$ from the silicone backing (calculate values) and negligible from Au. This results overall device aerial thermal masses of ~7.7 $mJ \cdot cm^{-2} \cdot K^{-1}$. The thermal mass of skin depends on the water content where thermal mass increases with skin hydration and water content[2]. For hydrated skin, the heat capacity is approximately 3.7 $J \cdot cm^{-3} \cdot$K-1, and the device aerial thermal mass of 7.7 $mJ \cdot cm^{-2} \cdot K^{-1}$ is equivalent to the aerial thermal mass of skin with a thickness of 20.8 μm.

Supplementary Note 4: Water vapor permeability test

Water permeability tests followed the ASTM E96 - 95 standard, and involved evaluation of e-TLC devices (thicknesses of 80 μm, 50 μm and 30 μm) and a commercial Feverscan™ device (LCR Hallcrest; polyester covering film ~75μm, liquid crystal layer ~10-50μm, black backing layer ~10-20μm and graphic print layer ~10-20μm). The experiments involved sealing the tops of identical jars, each containing a fixed amount of desiccant (97% anhydrous calcium sulfate and 3% cobalt chloride), with the devices under test. Control samples consist of jars without any seal on top. Diffusion of water vapor through the devices from the

surrounding ambient air causes increases in weight, due to uptake by the desiccant. All jars were placed in a room that has consistent temperature (~22ºC) and humidity (~50%). The weight gain of each jar was recorded at the same time of day on a balance that has precision of 0.1mg. By this test, after a 4-day period, the weight of the jar sealed by the Feverscan^{TM} remains unchanged, consistent with negligible water permeation. By contrast, weight of the jar with the 80 μm e-TLC device increases by an amount that is nearly half (41%) of that compared to the control. The 50 μm and 30 μm e-TLC devices exhibit weight increases that are greater than half of the control, i.e. 60% and 62%, respectively. These results indicate that our formulation of PDMS, at the thicknesses used in our devices, provide only minor barriers to moisture, particularly when compared to conventional analogs.

Supplementary Note 5: Sensor response time

The TLC dot array is embedded in between two PDMS layers. The thickness and thermal properties of the black PDMS substrate and the TLC layer will both determine the heat transfer rate from the skin to the top of TLC layer. The effect from the top encapsulation elastomer is neglected to simplify the model.

A warm ethylene glycol bath heats up the entire device from the backside of black PDMS substrate. The in-plane dimensions of the elastomer layer are much larger than its thickness such that the heat flux is mainly along the thickness direction, which can be represented by a one-dimensional heat transfer model described elsewhere. [1]

The sensor response time is defined by the time at which the sensor temperature increase T_{sensor} reaches 90% of T_0 . For 30μm black PDMS and 25μm TLC layer as used in the experiment, the response time is predicted to be ~30ms. These agree reasonably well with the experimentally measured sensor response time (for $T_{sensor} = 0.9T_0$) of 33 ms.

Supplementary Note 6: Color and temperature extraction process

The only parts of TLS sensor that are temperature sensitive are the liquid crystal dots. Finding them in the image and separating from black elastomer background is necessary first stage in temperature extraction process. This is a typical computer vision problem (OpenCV http://opencv.org/). The essential steps of the process are illustrated in Fig. 3a. First frame show the original picture of 7x7 area of the sensor array. Second is the output of Gaussian filter which reduce noise through image smoothing. Gray scale (third frame) format is required input for adaptive threshold (fourth frame). Adaptive threshold is the robust algorithm that is aware of the illumination non-uniformity at different parts of the image. The output is the binary mask containing value “1” at bright areas and “0” elsewhere. Small speckles from the defects are visible here as well. They are removed with the two step erode/dilate process. Erode (fifth frame) shrink the white areas in frame four by removing few pixels at the border. Due to the small size of the defects they vanish completely. Dilate step (sixth frame) expand the white regions back restoring area of interest by adding the same amount of pixels removed in the previous step. List of contours can be extracted from this “clean”

image (seventh frame). Every contour is enclosing a single temperature sensitive dot. The shape of the dot is closely reminiscent to circle. The obvious choice for dots position detection is the OpenCV's “enclosing circle” function which take a contour as an input. Last frame is the superposition of the original image and the set of corresponding positions (red dots) and enclosing circles (cyan rings).

Typical output of the digital camera is red-green-blue (RGB) color map. Intensities of all colors are affected by illumination conditions during the experiment. Converting to hue-saturation-value (HSV) color space make analysis more resilient to the change in lightning due to the fact that intensity now is encoded in value channel and color is in hue and saturation channels. In order to track the color change only hue and saturation are of interest. Figure 3b show the calibration we use to convert the colors into temperature. The dots plotted are positioned at corresponding hue/saturation values and painted with their hue value. Background is the temperature evaluated from them with two dimensional linear fit.

Supplementary Note 7: Steady-state thermal conduction model for prediction of thermal conductivity

A Cartesian coordinate system is set such that the origin is located at the center of the top surface of PDMS, as shown in Figs. S8a and S8b, where the schematic illustrations of the device geometry, from both the 3D and cross-sectional views, are presented. FEA indicates that the ultrathin e-TLC dots (~20 μm) have negligible effects on the temperature distributions, and thus are not considered in the analytic model. The skin layer (homogenized from real skin and

the underlying tissues, with the thickness >2 mm) are usually much thicker than the PDMS layer (with a thickness of ~60 μm), such that it can be considered as infinitely thick. The steady-state heat conduction equation is $\partial^2 T/\partial x^2 + \partial^2 T/\partial y^2 + \partial^2 T/\partial z^2 = 0$ for both the PDMS and skin, where *T* is the temperature. The square shaped resistor ($a_{Resistor} \times b_{Resistor}$) serves as the heat source, with the heat generation *Q* that pumps into the PDMS and skin. This can be modeled as a surface heat flux ($q_0 = Q/(a_{Resistor} b_{Resistor})$) for the bilayer system, i.e., $q_0 = q_{zPDMS}\big|_{z=-H_{PDMS}} - q_{zSkin}\big|_{z=-H_{PDMS}}$ for the region occupied by heat source. The free, top surface of the PDMS has natural convection with the surrounding air (T_∞), i.e., $q_{zPDMS}\big|_{z=0} = h(T - T_\infty)$, with *h* denoting the heat transfer coefficient. The continuity conditions include [*T*]=0 and [q_z]=0 across the PDMS/skin interface, where []=0 stands for the jump across the interface. By adopting the approach of double Fourier transform, the temperature at the sensor plane ($z = -H_{Sensor}$) is obtained as

$$T_{Sensor-layer} = T_\infty + \frac{4q_0}{\pi^2 k_{PDMS}} \cdot \int_0^\infty \cos(\omega x)\,\mathrm{d}\omega \int_0^\infty \frac{\sin\frac{a_{Resistor}\omega}{2} \sin\frac{b_{Resistor}\zeta}{2} \left(\mathrm{e}^{\eta H_{Sensor}} + \frac{k_{PDMS}\eta - h}{k_{PDMS}\eta + h} \mathrm{e}^{-\eta H_{Sensor}} \right) \cos(\zeta y)\,\mathrm{d}\zeta}{\omega\zeta\eta \left[\left(1 + \frac{k_{Skin}}{k_{PDMS}} \right) \mathrm{e}^{\eta H_{PDMS}} - \frac{k_{PDMS}\eta - h}{k_{PDMS}\eta + h} \left(1 - \frac{k_{Skin}}{k_{PDMS}} \right) \mathrm{e}^{-\eta H_{PDMS}} \right]}, \quad (3)$$

where the subscripts ‘PDMS’ and ‘skin’ denote the PDMS and skin, respectively; *k* is the thermal conductivity. Eq. (S3) corresponds to the temperature solution of the forward thermal conduction problem, given the thermal conductivity of the skin layer. The parameters adopted in experiments include $a_{Resister}$=$b_{Resister}$=0.5

mm, h=5 W·m^{-2}K^{-1}, H_{sensor}=30 μm, H_{PDMS}=60 μm, k_{PDMS}=0.16 W·m^{-1}K^{-1}, and the thermal diffusivity α_{PDMS}=1.07 m^2·s^{-1}. For a representative value of k_{skin}=0.31 W·m^{-1}K^{-1} and Q=3.8 mW, the distribution of temperature at the sensor plane, as given by Eq. (S3), is shown in Fig. S8c, which agrees reasonably well with FEA results (Fig. S8d). The temperature profile along the x axis (in Fig. S8e) is in quantitative agreement with the FEA results. The relatively large discrepancy at the center region is mainly attributed to the assumption of homogenious heat generation q_0 through the entire heater, adopted for the aim of model simplification. Fig. S8e also shows the temperature gradient is obvious in the region within a distance of ~4 mm from the heater center. For the sensors far from the heater (0.5 by 0.5 mm), the temperature distribution can be approximated by the simple solution of a point heat source, i.e.,

$$T_{Sensor-layer} \approx T_{\infty} + \frac{Q}{2\pi k_{Skin} r}, \tag{4}$$

where the ultrathin PDMS layer is neglected, and $r = \sqrt{x^2 + y^2}$ is the in-plane distance from the origin. Fig. S8e demonstrates that this approximate solution has very good accuracy for $r \geq a_{Resister}/2$. This simplified solution is adopted to predict the thermal conductivity of skin by fitting the temperature data from the e-TLC device, as shown in Fig. 5a for an example with $T_{\infty} = 33.9\ ^{o}\mathrm{C}$ and $Q = 3.83\ \mathrm{mW}$. Fig. 5b demonstrates the prediction of thermal conductivity for the calibration experiment, in which the water/ethylene glycol solutions with different mixing ratios are adopted to mimic real skin in different hydration levels. The

thermal conductivities predicted by the current model agree fairly well with those reported in the literature (MEGlobal, Ethylene Glycol Product Guide).

Supplementary Note 8: Transient thermal conduction model for prediction of thermal diffusivity

To simplify the analyses for the transient thermal conduction problem, we continue to assume that the heater is a point heat source. Consider that the heater is turned on at time t=0, the induced transient temperature solution is given by

$$T_{Sensor-layer}(t) \approx T_{\infty} + \frac{Q}{2\pi k_{skin} r} erfc\left(\frac{r}{\sqrt{4\alpha_{skin} t}}\right), \quad (5)$$

where α_{skin} is the thermal diffusivity of the skin, and $erfc(x)$ is the complementary error function. For the representative value of k_{skin}=0.31 W·m^{-1}K^{-1}, α_{skin}=1.14 m^2·s^{-1}, and Q=3.8 mW, the time dynamic temperature given by Eq. (S5) agree remarkably well with FEA results, as shown in Fig. S8f, for three different points (with a distance of 0.5, 1.0 and 2.0 mm from the origin).

Based on Eq. (S5), we can determine the thermal diffusivity based on the transient temperature data from the e-TLC device, even when the power is unknown (e.g., when the wireless system is adopted to power the heater). Fig. 5d gives an example of temperature profile at the sensor with a distance of 0.5 mm from the heater, where the analytic curve with the thermal diffusivity of 0.43x10^{-7} m^2/s gives the best match with the experimental data. Fig. 5e demonstrates the predictions of thermal diffusivity for the calibration experiment,

which agree reasonably well with those reported in the literature (MEGlobal, Ethylene Glycol Product Guide).

Supplementary Note 9: Mathematical modeling of reactive hyperemia

A two-dimensional (2D), transient, heat transfer model of human wrist was developed, which considers the various tissues surrounding the ulnar artery, and quantitatively characterizes the heat exchange between the blood flow and the surrounding tissues. Figure S10a and S10b show the schematic illustration of the tissue geometry, in which a circular cross section is adopted for the wrist to simplify the analyses. The blood at body temperature flows through the circular artery embedded in the fat layer, heating the surrounding tissues. The heat exchange between the blood flow and the fat layer across the artery wall is described with a heat convection model [2], which assumes the exchanged heat flux (q) to be proportional to the blood flow rate, i.e.

$$q = \frac{\rho_b c_{pb} \omega_b(t)}{\pi D_{artery}} \left(T_{body} - T_s \right), \tag{6}$$

where ρ_b, c_{pb}, $\omega_b(t)$ are the density, specific heat capacity, and time-dependent flow rate of the blood; D_{artery} is the diameter of the artery; T_{body} and T_s are the body temperature, and the temperature of fat at the artery wall, respectively. Due to the heating of the blood flow, the temperature distributes non-uniformly in these tissues, which is governed by the temporal heat conduction equation of $\rho_j c_j \frac{\partial T_j}{\partial t} = k_j \left(\frac{\partial^2 T_j}{\partial x^2} + \frac{\partial^2 T_j}{\partial y^2} + \frac{\partial^2 T_j}{\partial z^2} \right)$ (j=1..4), with the subscript representing different tissues (with skin as j=1, fat as j=2, muscle as j=3, and bone as j=4). The free,

outer surface of the skin has natural convection with air, which usually cools down the skin due to a lower room temperature than body temperature. The interior bone layer is assumed to maintain the core-temperature (close to the body temperature T_{body}).

The modeling of occlusion involves two steps, starting from the simulation of the steady-state heat conduction in the various tissues due to constant heating of blood flow, corresponding to the stage of pre-occlusion (Stage I). With the steady-state solution as an input, we further simulate the temporal changes in temperature distributions due to the application and release of occlusion, corresponding to the stage of vascular occlusion (Stage II) and reperfusion (Stage III), respectively. Based on previous experimental data, the temporal variation of blood flow during these different stages can be well described by the following piecewise function [2,3]

$$\begin{aligned}
&\omega_b^I(t) = \omega_0,\ t \le t_{occ,st} \\
&\omega_b^{II}(t) = (\omega_0 - \omega_s)\exp(-t/\tau_0) + \omega_s,\ t_{occ,st} < t \le t_{occ,end} \\
&\omega_b^{III}(t) = \begin{cases} (\omega_{\max} - \omega_s)\sin^2\left[\pi(t - t_{occ,end})/(2t_{dw})\right] + \omega_s,\ t_{occ,end} < t \le (t_{occ,end} + t_{dw}) \\ (\omega_{\max} - \omega_f)\exp\left[-(t - t_{occ,end} - t_{dw})/\tau_h\right] + \omega_0,\ t > (t_{occ,end} + t_{dw}) \end{cases}
\end{aligned} \quad , \qquad (7)$$

where ω_0 represents the baseline blood flow; ω_s is the blood perfusion after the occlusion is applied for a sufficiently long time, 160 s in the case of experiments here; ω_{max} is the maximum hyperemic blood flow; τ_0 is a time constant depicting the falling speed of blood flow after occlusion is applied; t_{dw} is the time required to reach the maximum hyperemic blood flow after the release of occlusion; τ_h indicates the rate at which the blood flow returns to the baseline value during the reperfusion; $t_{occ,st}$ and $t_{occ,end}$ denote the starting and ending times of the

occlusion, respectively. Except for $t_{occ,st}$ and $t_{occ,end}$, which are known in experiments ($t_{occ,st}$=0 s, $t_{occ,end}$=160 s), there are six parameters in this model of reactive hyperemia which can be varied to simulate the temperature history of blood perfusion. The aim of the thermal analyses is to obtain an optimized set of parameters that can minimize the average difference between the simulations and experiment data of temperature-time profile at those sensors with a distance ≤7 mm from the artery (Fig. 6g). The baseline blood flow ω_0 does not involve the occlusion process, and therefore can be determined using the temperature value measured before the occlusion (Stage I). The blood flow ω_s and time parameter τ_0 (only related to Stage II) are determined by the measured temperature-time profile during Stage II, and the other three parameters (ω_{max}, t_{dw} and τ_h) are determined by the data during Stage III. In total, there are six parameters in our simulations, i.e., ω_0, $\alpha=\omega_s/\omega_0$, $\beta=\omega_{max}/\omega_0$, τ_0, t_{dw} and τ_h, whose ranges are listed in Supplementary Table 1, based on reported experiments [2,3]

Finite element analyses (FEA) were adopted to solve the above transient heat transfer equation, and determine the temperature distribution numerically. 4-node linear heat transfer elements were used, and refined meshes were adopted to ensure the accuracy. The boundary conditions include the prescribed temperature ($T=T_{body}$) in the bone layer, the heat convection at the artery wall with blood flow of body temperature (i.e., Eq. (S6)), and the natural convection at the outer surface of skin with air of room temperature (~27.0 ^{o}C). The geometric and thermal-physical properties of various tissues are given in Supplementary Table 2. For the reactive hyperemia model described above, the baseline blood

flow rate is determined as ω_0=30 mL/min (19.6 cm/s for a vessel diameter of 1.8 mm), which could minimize the difference between FEA and experiment, i.e., the variance, as shown in Fig. S10c. Based on ω_0=30 mL/min, the calculated temperature decay from the artery at the steady state indeed agree well with experiment data (Fig. S10d). To minimize the temperature variance during stage II (Fig. S10e), the blood flow ω_s and time parameter τ_0 are determined as ω_s=1.5 mL/min and τ_0=2 s. Similarly, the other three parameters corresponding to stage III can be obtained as ω_{max}=90 mL/min (58.8 cm/s), t_{dw}=15 s and τ_h=35 s. For this set of parameters, the temperature-time profile obtained from FEA agrees reasonably well with the experiment results (Fig. 6g) for all the sensor points close to the artery.

Supplementary References

1 Webb, R. C. *et al.* Ultrathin conformal devices for precise and continuous thermal characterization of human skin. *Nat. Mater.* **12**, 938 (2013).

2 Deshpande, C. *Thermal analysis of vascular reactivity MS thesis*, Texas A&M University, (2007).

3 Akhtar, M. W., Kleis, S. J., Metcalfe, R. W. & Naghavi, M. Sensitivity of digital thermal monitoring parameters to reactive hyperemia. *J. Biomech. Eng-T. Asme.* **132,** 051005 (2010)

4 Fiala, D., Lomas, K. J. & Stohrer, M. A computer model of human thermoregulation for a wide range of environmental conditions: The passive system. *J. App. Physiol.* **87**, 1957-1972 (1999).

5 Song, W. J., Weinbaum, S., Jiji, L. M. & Lemons, D. A combined macro and microvascular model for whole limb heat transfer. *J. Biomech. Eng-T. Asme.* **110**, 259-268 (1988).

6 Sieg, P., Hakim, S. G., Bierwolf, S. & Hermes, D. Subcutaneous fat layer in different donor regions used for harvesting microvascular soft tissue flaps in slender and adipose patients. *Int. J. Oral. Max. Surg.* **32**, 544-547 (2003).

7 Shen, H. *et al.* A genomewide scan for quantitative trait loci underlying areal bone size variation in 451 Caucasian families. *J. Med. Genet.* **43**, 873-880 (2006).

8 Shima, H., Ohno, K., Michi, K. I., Egawa, K. & Takiguchi, R. An anatomical study on the forearm vascular system. *J. Cranio. Maxill. Surg.* **24**, 293-299 (1996).

9 McCartney, C. J. L., Xu, D., Constantinescu, C., Abbas, S. & Chan, V. W. S. Ultrasound Examination of Peripheral Nerves in the Forearm. *Region. Anesth. Pain. M.* **32**, 434-439 (2007).

10 Kathirgamanathan, A., French, J., Foxall, G. L., Hardman, J. G. & Bedforth, N. M. Delineation of distal ulnar nerve anatomy using ultrasound in volunteers to identify an optimum approach for neural blockade. *Eur. J. Anaesth.* **26**, 43-46 (2009).